express
polymer letters

Research article

A novel photocatalytic sheath/core bicomponent fibre for severe acute respiratory syndrome coronavirus inactivation

Widtawad Reantong[1], Siriluk Chiarakorn[1] , Pornsawan Leangwutwong[2]* ,
Akanitt Jittmittraphap[2] , Nanjaporn Roungpaisan[3] , Natee Srisawat[3]

[1]Environmental Technology Program, School of Energy, Environment and Materials, King Mongkut's University of Technology Thonburi, 126 Pracha Uthit Rd, Bang Mot, Thung Khru, 10140 Bangkok, Thailand
[2]Department of Microbiology and Immunology, Faculty of Tropical Medicine, Mahidol University, 420/6 Ratchawithi Road, 10400 Ratchathewi Bangkok, Thailand
[3]Department of Textile Engineering, Faculty of Engineering, Rajamangala University of Technology Thanyaburi, 39, M1 Rangsit – Nakhon Nayok Rd, Khlong Hok, Khlong Luang District, 12110 Pathum Thani, Thailand

Abstract. The coronavirus disease of 2019 (COVID-19) has become a global pandemic, leading to severe health issues such as pneumonia, organ failure, and death. Face masks made of non-woven textiles have been widely used to protect against SARS-CoV-2, but concerns arose regarding the potential infection from contaminated masks. To address this, titanium dioxide, a photocatalyst, shows promise in antimicrobial applications, including virus inhibition. This study explores the development of a sheath-core bicomponent fibre with a polypropylene core and a sheath containing an Ag and Zr *co*-doped TiO_2 photocatalyst (AZT). Zr-Ag-TiO_2 The fibres were produced using a double-extrusion spinning system, and the effects of the sheath-core ratio (50:50 and 80:20 w/w) and AZT content (1–3 wt%) on mechanical and antiviral properties were analysed. The fibres demonstrated improved mechanical strength and thermal stability, with the highest anti-SARS-CoV-2 activity (99.91%) observed in fibres with 2 wt% AZT at a 50:50 ratio after 30 min of fluorescent irradiation.

Keywords: antimicrobial properties, photocatalytic activity, nanocomposite, textile composite, bicomponent polymer fibre, modified titanium dioxide

1. Introduction

Coronavirus disease 2019 (COVID-19) is a viral illness caused by the coronavirus strain SARS-CoV-2. It was first identified in December 2019 in Wuhan, China, and has since become a global pandemic. COVID-19 primarily spreads through respiratory droplets when an infected person coughs, sneezes, talks, or breathes and spreads through contact with surfaces or objects contaminated with the virus, followed by touching the face [1–3]. Common symptoms include fever, cough, shortness of breath, fatigue, muscle aches, headache, sore throat, loss of taste or smell, congestion, nausea, vomiting, and

diarrhoea. Symptoms range from mild to severe, but some individuals may be asymptomatic [4]. While many people recover without hospitalisation. COVID-19 continues to affect lives and strain health-care systems worldwide. Socially effective prevention measures include frequent handwashing, wearing face masks, practising physical distancing, avoiding large gatherings, and following guidelines and recommendations from health authorities. Personal protective equipment (PPE) plays an important role in preventing the transmission of COVID-19. Researchers reported SARS-CoV-2 can survive on surfaces and masks for 1–28 days [5]. This raises

*Corresponding author, e-mail: pornsawan.lea@mahidol.ac.th

concerns over the potential for infection from improperly handled, contaminated PPE. To overcome this obstacle, researchers have embedded antiviral substances into PPE to inactivate any contaminating viruses. This may result in less viral propagation and PPE that lasts longer, which would benefit any shortages occurring in the PPE supply chain.

In response to the current COVID-19 outbreak, anti-SARS-CoV-2 spun-bond fabrics and fibres were developed by coating disinfectants onto the surface of the fabric or fibre. Consequently, coating textiles with antiviral compounds may reduce the spread of respiratory infections through indirect contact. In this context, a variety of coating techniques for antivirus purposes have been developed, such as the vacuum method used for coating PP non-woven surgical face masks with copper oxide [6], and spray and dipping methods for coating NaCl on the non-woven microfiber cloth made, exhibited antiviral efficacy [7]. Coated fibres are effective at inhibiting the virus. In addition, fabrics coated with antiviral coatings, such as silver nanoparticles [8], organo-silane [9], and photocatalyst particles [10], which were coated by the dip-coat, pad-dry-cure and sputtering method on fibre or fabric, have been developed.

Unfortunately, wiping or washing can easily remove the disinfectant coating on surfaces. To overcome this limitation, disinfectant additives, such as silver nanoparticles and other photocatalysts (zinc oxide, titanium dioxide, zirconium dioxide [11, 12]), may be incorporated into the fibres during extrusion processing. In the textile field, modifications typically occur during the fibre-forming process. Recently, it has been possible to create antibacterial fibres by embedding antibacterial particles into polymers during the fibre-forming process. However, when the additive is embedded in the fiber matrix, its contact with microbes is limited, reducing its effectiveness. To address this, a novel bicomponent fiber melt-spinning technique places the photocatalyst in the sheath and the polymer in the core. Pivsa-Art S [13]. prepared the TiO$_2$ on RPET (recycling polyethylene terephthalate). Bicomponent multifilament yarns are responsible for their antibacterial properties. They exhibit high efficacy, and TiO$_2$ nanoparticles embedded with the RPET melt blend method used on multifilament yarns stay for longer periods of time. Furthermore, the use of TiO$_2$ particles for the formation of antibacterial bicomponent fibers has been highly resistant to bacteria.

TiO$_2$ photocatalysts frequently employ polymers to impart special functionality. Moreover, many articles report that photocatalysts have potential candidates for anti-SARS-CoV-2 under UV irradiation, such as titanium nanotubes (T_NTs) [14], and pure TiO$_2$ [15]. However, the disadvantage of TiO$_2$ is its wide bandgap (3.2 eV), and exhibits a relatively high rate of electron-hole recombination [16, 17]. To overcome these disadvantages the photocatalytic activity performance of TiO$_2$, first approach is to control the structure such as morphology crystal phase and surface area by doping single or *co*-doping metal and non-metal [18]. Many studies have currently reported that metal doping, such as Zr [19], Cr [20], Pd [21], Au [22], and Ag [23], can improve photocatalytic activity in to visible light. The *co*-doping of TiO$_2$ with Ag and Zr will be examined in this paper since each dopant metal component contributes differently to the increase in photoactivity. As previously mentioned [24], the synergistic effects of certain *co*-dopants can increase photocatalytic activity responses.

Thus, this article aims to modify the photocatalytic activity of TiO$_2$ by *co*-doping Ag and Zr via the solvothermal method. It is used as an additive to prepare sheath-core bicomponent fibre, whereas the PP was used as a polymer matrix. The effects of the S/C ratio and photocatalyst powder content on morphology, thermal stability, and mechanical properties were evaluated. The anti-SARS-CoV-2 efficacy of the bicomponent fibres was then examined following International Organization for Standardization No. ISO 18184:2019 [25].

2. Experimental section
2.1. Materials and reagents

Titanium tetrachloride (TiCl$_4$, 98%) was purchased from Shanghai Runwu Chemical Technology Co., Ltd. (China). Zirconium tetrachloride (ZrCl$_4$, 98%) and silver nitrate (AgNO$_3$, 99%) were purchased from Sigma-Aldrich. Ammonia solution (NH$_3$, 28–30%), hydrogen peroxide (H$_2$O$_2$, 30 mass%), and methylene blue (C$_{16}$H$_{18}$N$_3$SCl, 98%) were obtained from Merck. The polypropylene H561R (PP561R) supplied by HMC Polymers Co. Ltd. (Thailand) was used as a polymer matrix. The melt flow rate and the density of the PP matrix were 25 g/10 min (230 °C/ 2.16 kg) and 0.90 g/cm^3, respectively. For the SARS-CoV-2 inhibition test, Vero cells (Vero clone E6, Vero E6) CRL1586TM, Gibco Minimum Essential

Media (MEM; Gibco BRL), fetal bovine serum, glutamine, penicillin, and streptomycin were used according to ISO 18184:2019 [25]. All raw materials were employed without additional purification.

2.2. Preparation of bear-TiO₂ and *co*-doped TiO₂ photocatalysts

Bear-TiO₂ was synthesized by adding TiCl₄ into deionised water under stirring for 30 min. Precipitation of the TiCl₄ solution, adding ammonia solution with the final pH of the solution after precipitation was 7, the titanium gel was formed. The gel was washed with deionized water and separated by centrifuge and filtration until Cl ions were not detected with 0.1 M of AgNO₃. The gel was changed to a transparent yellow by adding an H₂O₂ solution with four times the number of moles of titanium, then transferred to a teflon-lined stainless-steel autoclave (250 mL) reactor for a solvothermal treatment in a hot air oven at 150±5 °C for 6 h to form a particle catalyst. The precipitated particles were filtered and washed with deionized water several times and then dried at 80±5 °C overnight. The dried particles were grinded to a fine powder by hand grinding.

For the preparation of the Zr and Ag *co*-doped TiO₂ (AZT), AgNO₃ and ZrCl₄ were used as Ag and Zr sources, respectively. This approach added the fixed Zr at 5% mole of TiO₂ into the titanium solution. The Zr was fixed at 5% mole of TiO₂. It shows the highest photocatalytic activity of the Zr doped TiO₂ from recent publication research [24]. Silver nitrate at 1, 3, and 5 mole% of titanium was added to the solution and stirred for one hour to release gas. The photocatalyst was formed by solvothermal treatment under the same conditions as bare-TiO₂. The AZT particles were identified as A*x*ZT when *x* is the concentration of Ag in a percent mole unit.

2.3. Catalyst characterizations

The fabrication of photocatalyst particles was investigated using several analytical characterization techniques. Scanning electron microscopy with energy-dispersive X-ray spectroscopy measurements (SEM-EDX) was used to identify the morphology and chemical composition of samples. The structural phase and crystallinity structures were characterized by using an X-ray diffractometer with CuK$_\alpha$ radiation (λ = 1.5406 Å) at a 40 kV source, recording a 2θ range from 20–80°. The Joint Committee on Powder Diffraction Standards (JCPDS) database was

used to identify the peak. The average crystallite size was determined using the Scherrer formula (Equation (1)) [18]:

$$D = \frac{K\lambda}{\beta_{hkl}\cos\theta} \qquad (1)$$

where D is the average crystallite size [nm], K is the shape factor (0.89), λ is the incident X-ray wavelength (1.5406 Å). The optical properties were investigated by using a UV-VIS-NIR spectrophotometer at a wavelength range of 300–700 nm. The band gap energy of catalysts was estimated using the Taur-plot method by plotting the $(\alpha h\upsilon)^{1/2}$ *versus* the photon energy ($h\upsilon$) [18].

2.4. Photocatalytic decolorization of methylene blue

The photocatalytic activity experiments of synthesized photocatalyst particles were carried out by investigating the decolorisation of methylene blue dye (MB) under a fluorescent lamp (fluorescent 18 W, Philip lamp) in a closed wooden box chamber. The light intensity in a closed reactor was around 500–700 lux. In the experiment, 0.02 g of photocatalyst was dispersed in particles in 100 mL of $1\cdot10^{-5}$ M methylene blue solution. The absorption is carried out in the dark with continuous stirring at room temperature (28–30 °C) until the adsorption equilibrium is reached. The photocatalytic reaction was evaluated with the new methylene solution, and the light was turned on. To show the photocatalytic performance of a catalyst that has already been synthesised, the photolysis process of MB was also carried out without any catalyst. The photocatalytic degradation of MB was investigated by using UV-visible spectroscopy at 665 nm (λ_{max}) [18]. The photocatalytic efficiency was calculated using the following expression from Equation (2):

$$\text{Photocatalytic efficiency} = \frac{C_0 - C_t}{C_0}\cdot 100\% \qquad (2)$$

when C_0 and C_t are the MB concentrations at the initial time and measuring time, respectively.

2.5. Preparation of polypropylene/AZT particles composites

The highest photocatalytic efficiency was used to prepare PP/AZT particle composites fiber. The PP/AZT composites as a fiber sheath were prepared by compounding PP561R with AZT at 1–3 wt% in

a dry mixer chamber and transferring it into a twin-screw extruder. The temperature profiles were set at 130, 160, 180, 190, 210, 220, and 230 °C, and the die temperature was set at 230 °C with a screw speed of 95 rpm. The extruded polymer composites were cut with a cutting machine at a speed of 990 rpm.

2.6. Melt-spinning of PP/AZT bicomponent fibres

Sheath-Core (S/C) bicomponent fiber spinning was performed using a lab-scale double-extrusion fiber spinning system with 24 spinneret holes (HILLS, Inc., model LBTH) as shown in Figure 1. The 1–3 wt% of PP/AZT composite pellets were placed in extruder B (sheath extruder), and neat PP was placed in extruder A (core extruder). The temperature profiles of both extruders were set at 210, 220, and 230 °C, and the temperature of the melt pumps was set at 235 °C. The throughput rate was set at 0.2 g·hole^{-1}·min^{-1}. The effect of the S/C ratios (50/50 and 20/80 (w/w)) on fibre formation and properties were determined. The samples were labelled PP*x*/50:50 and PP*x*/20:80, where *x* represents the sheath's AZT content [wt%]. For control samples, solid PP and solid PP/AZT composite fibers containing 1 wt% AZT (PP1), 2 wt% AZT (PP2), and 3 wt% AZT (PP3) were used. The extruded fibers were collected on bobbins at a fixed speed of 1000 m/min.

2.7. Fiber characterization

The fibre morphology was examined with an optical microscope (Olympus CX41, Panasonic) at a magnification of 10×. The fibre cross-section microtome plate method was used to make fibre cross-section specimens for the tests. The fibre samples were packed into plates and cut off with a sharp razor blade. In addition, the elemental composition and depth profiling surface analysis of the bicomponent fibres were characterised by scanning electron microscopy with energy-dispersive X-ray spectroscopy (SEM-EDX). A differential scanning calorimeter (Thermo Scientific model NETZSCH DSC 200 F3) was used to examine the thermal properties of the bicomponent fibers. To remove the thermal history, the fiber samples were heated from room temperature to 200 °C at a rate of 10 °C/min for 3 min. Then, the samples were cooled to 30 °C at a cooling rate of 10 °C/min and heated again to 200 °C at a heating rate of 10 °C/min under nitrogen flow. The melting temperature (T_m), melting enthalpy (H_m), and percent crystallinity were examined according to the differential scanning calorimetry (DSC) data. The percentage of crystallinity (X_c) of the samples was calculated according to Equation (3) [26]:

$$\text{Crystallinity } (X_c) = \frac{\Delta H_m}{\Delta H_m^\circ} \cdot 100\% \tag{3}$$
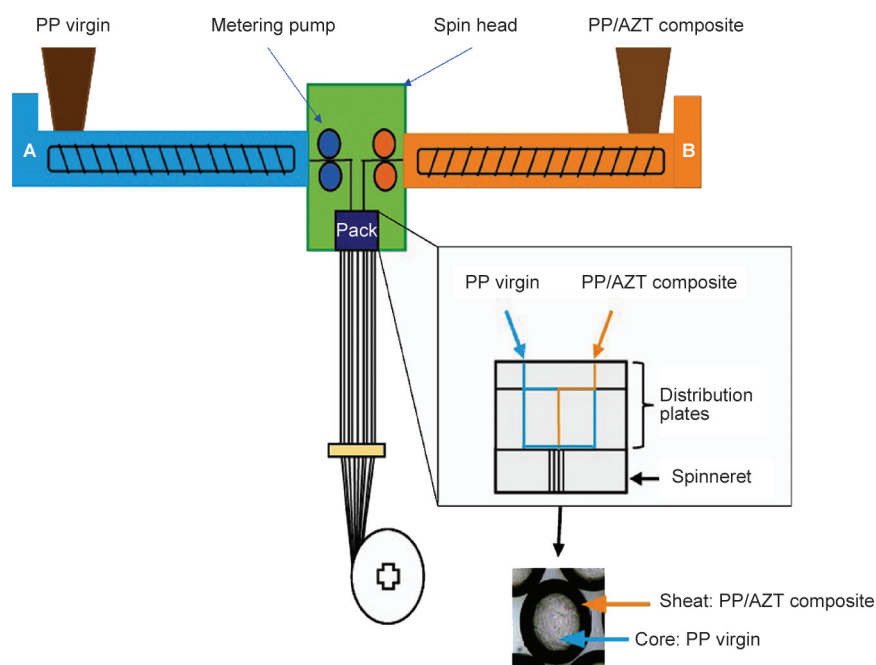
Figure 1. Sheath/core bicomponent process with lab-scale, double-extrusion fiber spinning system (HILLS Inc., model LBTH).

where ΔH_m is the enthalpy of crystallization of the tested fibre samples calculated from the area of the endothermic melting peaks and ΔH_m° is the extrapolated value of enthalpy corresponding to the melting of 100% crystalline PP, which was reported as 207.1 J/g [26].

The tensile strength test of the fibres was modified according to the ASTM D 3822-01 standard method. A universal testing machine was used with a load cell of 10 cN capacity with a gauge length of 20 mm and a test speed of 20 mm/min. The pressure was set to 0.5 cN/dtex and the testing temperature was maintained at 25 °C. The tensile strength of the fibers was calculated using the measured diameters.

2.8. Photocatalytic activity against severe acute respiratory syndrome coronavirus 2

Vero cells (Vero clone E6, Vero E6) CRL1586TM were cultured in minimum essential media (MEM; Gibco BRL) with 10% heat inactivated FBS, 1% glutamine, 100 U/mL penicillin, and 100 g/mL streptomycin. Severe Acute Respiratory Syndrome Coronavirus 2 (SARS-CoV-2) (locally isolated strain Delta variant (B.1.617.2)) was propagated and titrated in Vero cells using the 50% tissue culture infectious dose assay (TCID50). The virucidal activity of the bicomponent fiber samples was determined using a modified test method according to ISO 18184:2019 [25]. In this testing, methods are used to determine the antiviral activity of the textile product, including woven, non-woven, knitted fabric, yarns, active wear, socks, daily wear, and health products such as scrubs, masks, surgical clothes, and other home textiles. The samples were cut into 20×20 mm pieces and tested for their activity against SARS-CoV-2. Bicomponent fibers were inoculated with 200 mL of virus at a concentration of $2 \cdot 10^5$ cell/mL and incubated for 15 min at 25 °C and for 30 min at 30 °C. They were then neutralized and filtered after 15 and 30 min of contact. The light source was a fluorescent lamp (fluorescent 18 W, Philip lamp) with an intensity of around 500–700 lux in a glass-closed chamber. The filtrate was subjected to 10-fold serial dilutions, applied in quadruplicate to 96-well plates containing Vero E6, and incubated for 3–4 days at 37 °C. The Reed-Muench method was used to quantify the number of remaining viruses following the appropriate incubation time. Many controls that are essential to test validity are included in our tests. When a sample is recovered just after the virus is

added to the virgin PP (time zero), the viral recovery control measures the initial amount of virus. For the test to be considered genuine, there must be a sufficient similarity in the quantity of infectious virus recovered from the virgin PP both immediately after inoculation and after the contact period. The antiviral activity was then calculated according to Equation (4) [25]:

$$M_v = \log_{10}(V_a) - \log_{10}(V_b) \qquad (4)$$

where M_v is the antiviral activity value, $\log_{10}(V_a)$ is the logarithm average of 3 infectivity titre values immediately after inoculation of the control specimen, and $\log10(V_b)$ is the logarithm average of 3 infectivity titre values immediately after inoculation of the test specimen. The antiviral performance of the textile product is considered good when the log value is between 2 and 3. If the log value is greater than or equal to 3, then the antiviral is considered excellent.

3. Results and discussion
3.1. Photocatalyst materials characteristics
3.1.1. Color and morphology

The coloured particles of the produced photocatalysts, bare TiO_2 (T) and Ag and Zr *co*-doped TiO_2 (AZT) with Zr 5 mole% and Ag 3 mole% (A3ZT), are shown in Figure 2. On the inset picture the color of A3ZT is portrayed as pale grey, while the color of T is shown as dazzling white. When compared to the Ag 3% dopant loading, the doped TiO_2 with different Ag loadings of 1 and 5 mole% showed brighter and slightly darker colours, respectively (the images are not shown). The various hues of the photocatalyst have an impact on the light absorption characteristics. A photocatalyst's hue will vary depending on the doping agent's amount and ability to reflect and absorb light. The SEM image in Figure 2. shows that all the prepared photocatalysts have the same uniform spherical shape agglomeration. The A3ZT has a large particle agglomeration and a homogenous distribution compared to the bare TiO_2 particles. The estimated particle size was around 25–60 nm for AZT and 15–20 nm for bear-TiO_2. Hence, the effects of Ag and Zr dopants in the TiO_2 structure.

3.1.2. Crystallinity

X-ray diffraction (XRD) techniques were used to investigate the effects of Zr and Ag on the crystal structure and crystallite size of photocatalysts with
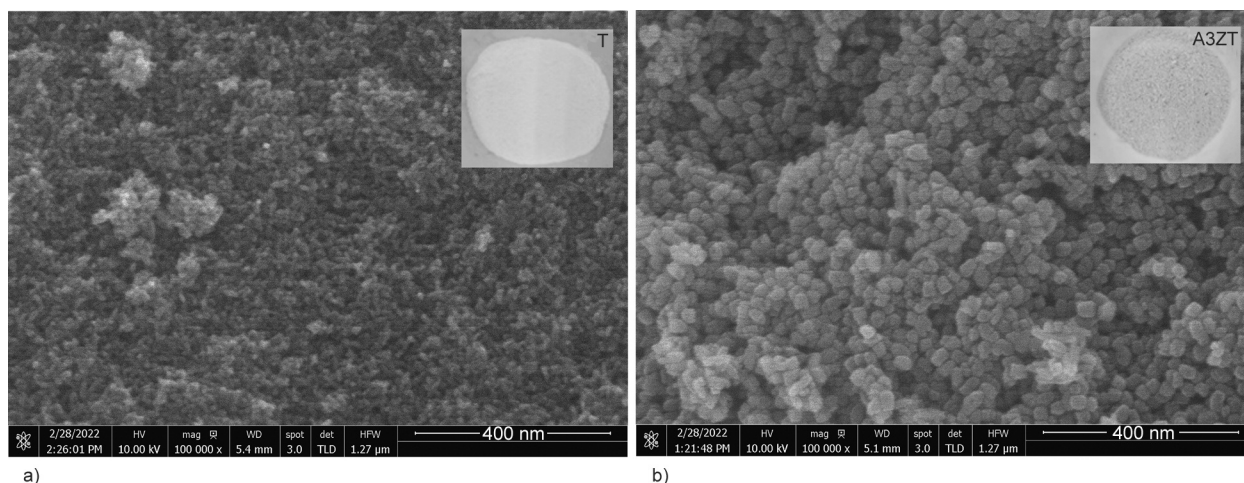
Figure 2. The surface morphology of a. TiO₂ (a), and (b). Ag-Zr *co*-doped TiO₂ with Ag 3 mole% of Ti (b), determined from SEM.

different loading levels of Ag at 1, 3, and 5 mole%. The Joint Committee on Powder Diffraction Standards (JCPDS) database with card no. 21-1272 [27], 43-0997 [28] and 04-0783 [28] as anatase crystal phase, silver dioxide crystal phase and silver nanoparticles, respectively. The XRD patterns of AZT, including bare TiO₂, Ag doped TiO₂, and Zr doped TiO₂ were shown Figure 3. All the diffraction planes correspond to anatase phase of TiO₂ with tetragonal body centered and having two forms of silver: Ag₂O and Ag on Ag doped TiO₂ and Ag and Zr *co*-doped TiO₂. However, no additional diffraction peak match with any Zr phase (JPCDS card no. 17-0923 and 37-1484 [29]), which mean that the anatase phase of TiO₂ with doped and *co*-doped remained unchanged and Zr was successfully incorporation in to TiO₂

matrix. This absence might be attributed to the good incarceration of Zr into Ti [19]. Hence, Ag and Zr were shown the different effects on crystal structure. The Zr doping can have an interstitial effect due to the fact that the ionic radius of Zr^{4+} (72 pm) is slightly bigger than that of Ti^{4+} (53 pm), so Zr^{4+} could be in interstitial. The other kind, the substitutional Zr^{4+} effect on TiO₂, is that Zr^{4+} ions will replace the Ti^{4+} ions in the crystal structure [24, 30]. Its effect on the lattice parameters and crystal size, accompanied by a shift of diffraction angle of the XRD peak (Figure 3b). In comparison to ZT with T, the samples gradually move slightly to lower angles as the doping Zr. The Ag dopant, Ag^+ (128 pm) has a larger radian than Ti^{4+}, which it cannot incorporate into the TiO₂ lattice [31, 32]. The rest of the Ag ended
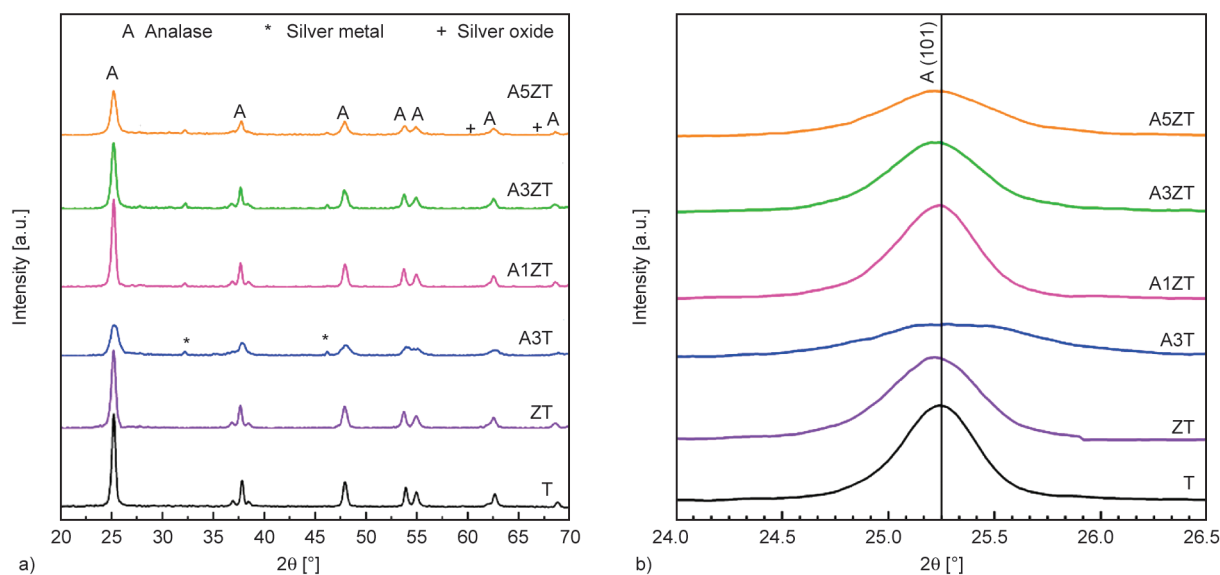
Figure 3. XRD pattens of T, single and *co*-doped TiO₂ (a) and displays the enlargement of (101) plane (b).

up as metallic silver and silver dioxide nanoparticles on the surface of the TiO₂. So, the Ag dopant can be moved to a lower degree of XRD, which shows that most of the Ag dopant was put on the surface of the TiO₂, as shown in Figure 3b. Figure 3b shows a shift in the diffraction peak of anatase 101, which is T, A3T, ZT, and A3ZT.

The crystalline size was calculated by using Scherrer equation at the principal diffraction peak at $2\theta = 25.1°$ [33]. The XRD pattern of pure TiO₂ display for 6 main peaks located at 25.3, 38.0, 48.2, 54.0, 55.1, and 63.0°, respectively, with planes of (101), (004), (105), (211), and (204) [27], respectively. The main diffraction peak (101) at 2θ at 25.3 (Figure 3b) slightly decreases with doping Ag. The average crystalline size of Ag-Zr *co*-doped TiO₂ with difference ration (0, 1, 3 and 5 mole%) was determined using XRD data show in Table 1. The crystals size decreases with increasing Ag ratio. This could be owing to an Ag has affected the TiO₂ crystal [32]. The lattice parameter was expanded with doped and *co*-doped

TiO₂ as defect in the crystal lattice. Consequently, the XRD results are clearly demonstrates successfully modifies TiO₂ by Ag and Zr *co*-dopant. In this study, the crystallite size of anatase TiO₂ has been changes. So, Zr and Ag loading through solvothermal synthesis were successfully added to a TiO₂ matrix and were the main factors affecting the crystallinity of TiO₂.

3.1.3. UV-visible spectroscopy

Figure 4a displays the results of doped and *co*-doped TiO₂, including pouring TiO₂ as a reference. According to the spectra, the absorbance of Ag-doped TiO₂ changes a lot at longer wavelengths and goes up a lot when it is exposed to fluorescent light. Due to surface plasmon resonance, a special optical characteristic of Ag when Ag nanoparticles interact with light, this may be the cause of this [31]. By doping Zr into the TiO₂, the optical absorption edges became bluer, which was caused by the re-placing of Zr⁴⁺ in the TiO₂ lattice. The AZT showed a noticeable red shift

Table 1. Morphologic and electronic properties of the synthesized photocatalysts.

Samples name	*d*-spacing at $2\theta = 25.3°$ at (101) plane	Lattice parameter (*a* = *b*, *c*) [Å]	Crystalline size [nm]	Band gap [eV[
T	1.8071	*a* = *b* = 2.0746, *c* = 5.0222	26.81	3.23
ZT	1.8083	*a* = *b* = 2.0754, *c* = 5.0431	17.49	3.08
A3T	1.8008	*a* = *b* = 2.0721, *c* = 5.0212	9.08	1.85
A1ZT	1.8078	*a* = *b* = 2.0744, *c* = 5.0407	19.66	2.85
A3ZT	1.8077	*a* = *b* = 2.0751, *c* = 5.0394	16.81	2.80
A5ZT	1.8066	*a* = *b* = 2.0760, *c* = 5.0351	14.94	2.79
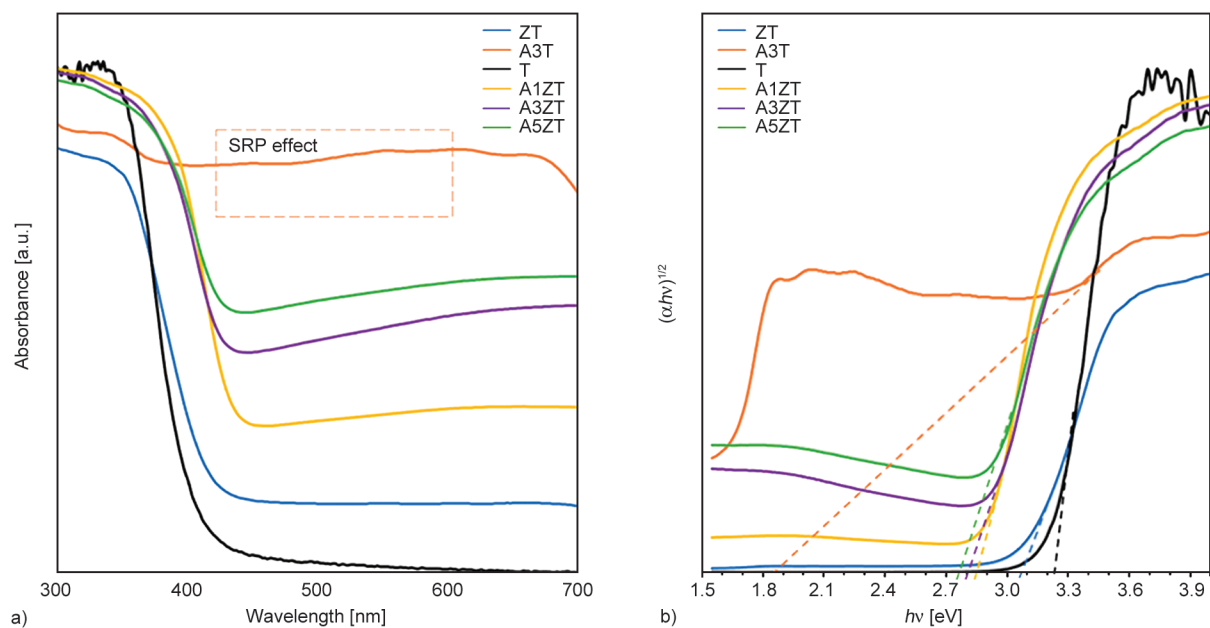
Figure 4. UV-visible spectra (a) and Tauc-plot (b) of T and AZT (varied Ag at 1, 3, and 5 mole%).

in the visible light range. This is because Zr traps electrons and slows down the recombination of electron/hole pairs, whereas Ag increases the absorbability of TiO_2 in visible light by narrowing the energy band gap. The visible light absorbance of A5ZT is higher than the sum of all the samples' visible light absorbances, except for Ag-doped TiO_2. This suggests that Zr and Ag have a synergistic effect on visible light absorption.

Figure 4b displays the band gap energies. This was computed from the Tauc equation, and the *n* value is 1/2 as TiO_2, a direct band gab energy [33]. All of the doped samples had a decrease in band gap energy. The band gap energy was reduced when doped with Ag and increased when Zr-doped TiO_2. Therefore, when considering single-dopant Ag, it shows the lowest band gap energy due to the effect of color and the surface plasmon resonance of silver. while the single-dopant Zr traps electrons, retards electron/hole pair recombination, and shows strong absorption in the blue region. When considering Ag and Zr *co*-doping with varying amounts of Ag, the TiO_2 optical band gap shifts to lower energy values (2.85, 2.80, and 2.79 with A1ZT, A3ZT, and A5ZT, respectively). This phenomenon has a synergistic effect.

3.1.4. Photocatalytic activity of sample
The degradation progress of MB was monitored with UV-VIS absorption spectra. In this experiment, the photocatalyst powder was stirred in the dark until adsorption equilibrium was reached for 3 h. Figure 5a shows the photo decolorization of the MB under fluorescent light in the presence of the investigated photocatalysts. After the light was turned on for 8 h, MB had a slight degradation of only 5.51%, which

is affected by the light photolysis. In Figure 5a, the result found under fluorescent irradiation was that all doped TiO_2 samples had higher degradation efficiency than virgin TiO_2 in the order of TiO_2 (18.99%) < A1ZT (50.35%) < A5ZT (72.60%) < A3ZT (93.53%). Interestingly, A3ZT exhibited the highest photocatalytic efficiency of 93.51% in 8 h, indicating its optimum concentration of Ag dopant for improvable photocatalytic activity. This is because the surface plasmon resonance of silver was performed. Another reason that should improve photocatalytic activity is that the Zr doping effect retards electron-hole pair recombination. The possible mechanism for photocatalytic degradation of the MB over bare TiO_2 with the doping of Zr, and Ag are presented in Figure 5b. When the AZT was activated with light, the synergetic effects on the thermos catalytic activity upon the silver oxide surface and the efficient electron-hole separation at the photocatalyst/ Ag_2O interface migrated to the Ti^{4+} site, where they were transferred to the conduction band and trapped by Zr to generate the superoxide radical, while H_2O molecules could be adsorbed by the positive hole placed in the valence band of TiO_2 to produce the hydroxyl radical. In the photocatalytic oxidation process, both superoxide (O_2^0) and hydroxyl (OH^o) radicals are potential oxidants that can strongly interact with the organic compound [34]. For this research, we are looking at the *co*-doped TiO_2 duo to show the synergy effect of the photocatalyst. From this result, Ag-Zr *co*-doped TiO_2 with Zr 5 mole% and Ag 3% mole was selected as an additive in bi-componence fiber. Because of its show the highest photocatalytic activity under fluorescents irradiation.
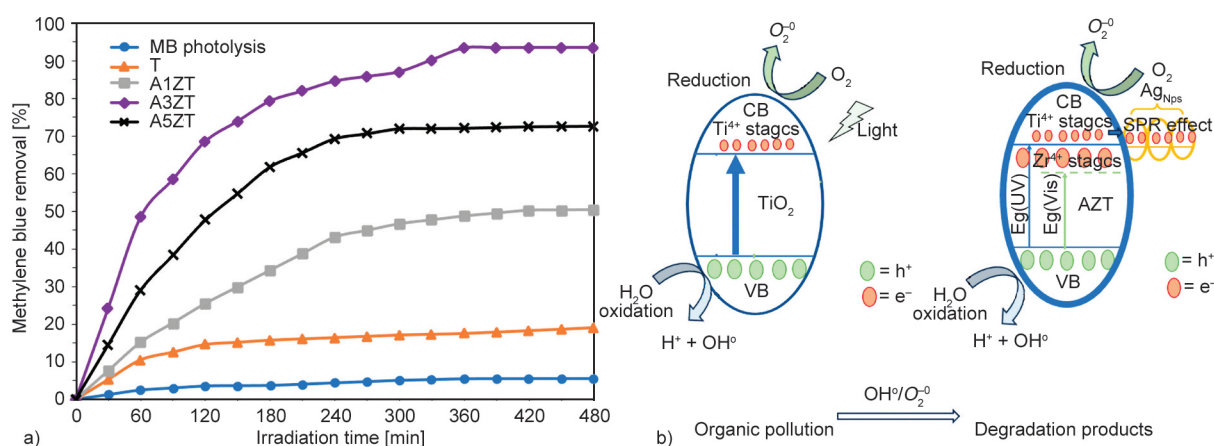
Figure 5. Photocatalytic degradation efficiency of T and AZT under fluorescent light irradiation (a), and schematic diagrams of the band energy structure and mechanism of photocatalytic degradation (b).

3.2. Photocatalyst bi-componence fiber characteristics

### 3.2.1. Spinnability, morphology, and chemical composition

PP fiber, PP composite fiber, and S/C bicomponent fiber were successfully fiber spin at a winder speed of 1000 m/min. The A3ZT was increased to 3 wt%, spinneret clogging was observed along with an inability to form fibers at all S/C bicomponent ratios. The morphology of the samples was examined using optical microscopes, as shown in Figure 6. The cross-section of the PP composite fiber with various A3ZT particles was shown to be poorly transparent. Poor transparency indicates that the A3ZT powder incorporated in the PP matrix may be dispersed in all matrices. The cross-section of the sheath-core bicomponent fiber exhibited a poorly transparent sheath containing A3ZT powder and the core exhibited light transmittance through the polymer materials. Similarly, the sheath-core bicomponent fiber with different S/C ratios had a different sheath thickness. The fiber thicknesses of virgin PP, PP1 and PP2 were 91.16±1.03, 74.34±1.64 and 58.09±8.39 μm, respectively. At the S/C ratio of 20:80, the sheath thickness of both concentration at 1 wt% Figure 6b and 2 wt% Figure 6e were approximately 6.11±0.33 and 6.26±2.57 μm, respectively. While at the S/C ratio of 50:50, the sheath thickness increased to about 17.40±0.31 μm for 1 wt% Figure 6c and 13.31±0.33 μm for 2 wt% Figure 6f, respectively.

When the sheath ratio increased, it was observed that the sheath thickness increased while the sizes of the fiber core decreased. The increase in sheath ratio affects the mechanical and thermal properties of the polymer [7]. The larger sheath area, the better photocatalytic antivirus activity.

The fiber properties were significantly affected by the prepared photocatalyst particle dispersion stage. A mixing procedure with a twin-screw extruder can be used to distribute and break up the agglomeration of A3ZT particles uniformly throughout the polymer matrix. The surface morphology and elemental composition on the surface of the fibers are shown in Figure 7. A pure PP fiber was shown to have a smooth surface, whereas fiber made with a sheath that contained A3ZT powder was not smooth on the surface. The result indicates that some A3ZT powder on the fiber had particle agglomeration on the surface, which was clearer in those containing 2 wt%, and the surface of the fibers was not smooth. Furthermore, the polymer containing a photocatalyst or any additive amicrobial filler fixed inside the polymer matrix will be inactive because of its inability to contact and react with microbes. Thus, the sheath-core fiber technique is the most effective way to improve the antibacterial properties of the fiber because it increases function, maintains the fiber properties, and reduces cost. The results indicated that the sheath PP composite with A3ZT powder exhibited effective photocatalytic activity, which was enhanced when
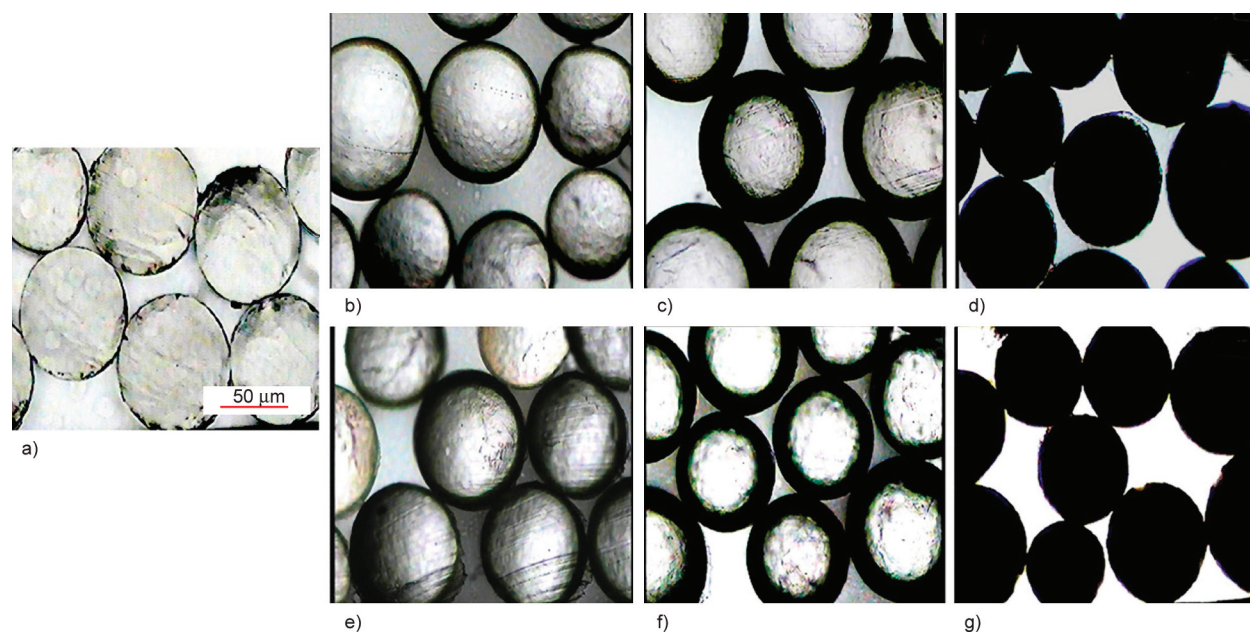
Figure 6. Micrography of the cross-section of free fall fiber with 10× magnification a) PP virgin, b) PP1/20:80, c) PP1/50:50, d) PP1, e) PP2/20:80, f) PP2/50:50, and g) PP2.
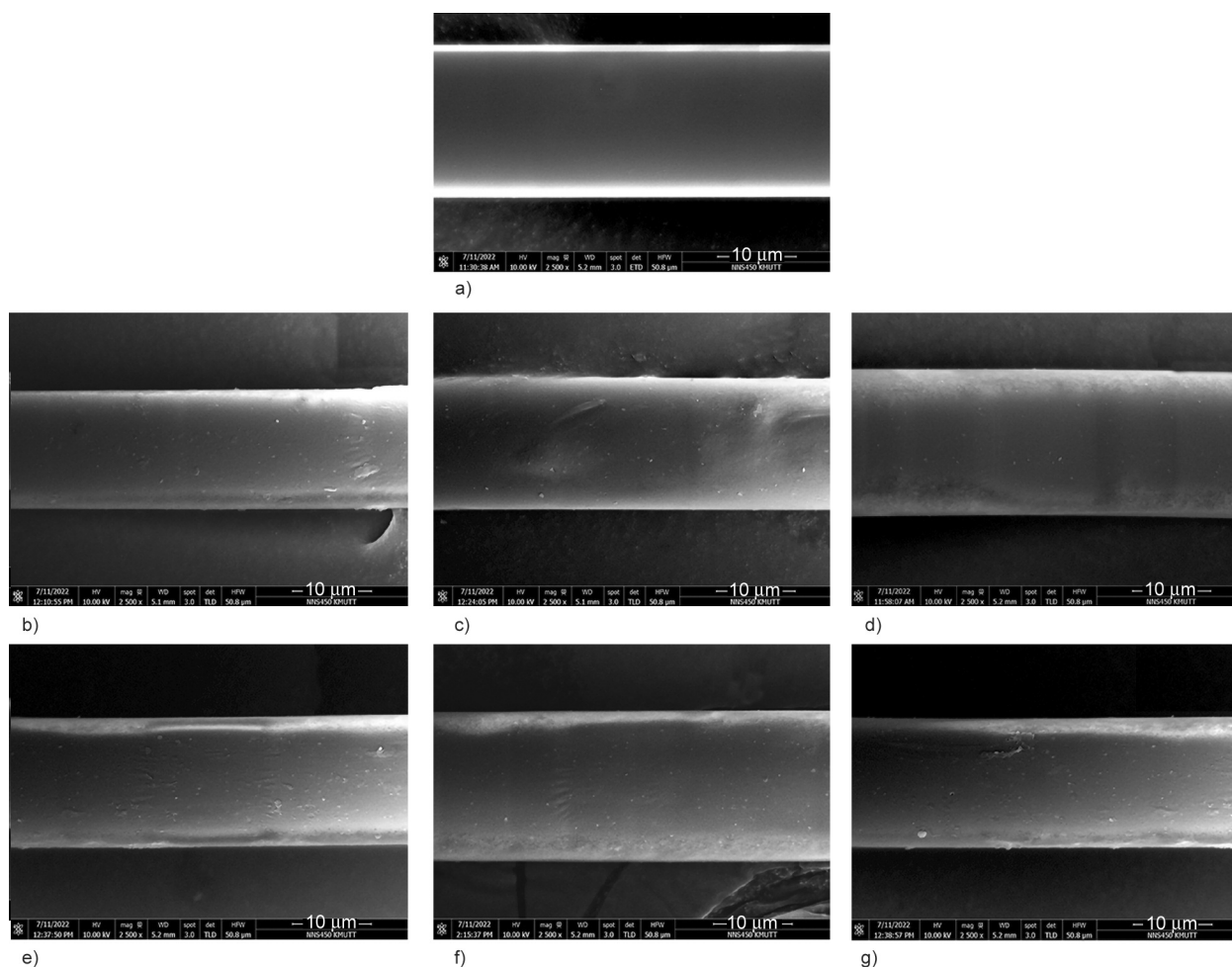
Figure 7. SEM magnification (2500×) images of the Sheath-Core bicomponent fibers prepared at different S/C ratios and A3ZT powder content: a) PP virgin, b) PP1/20:80, c) PP1/50:50, d) PP1, e) PP2/20:80, f) PP2/50:50, g) PP2.

A3ZT content was increased in the sheath and the composite was incorporated into the polymer, thus remaining for a longer time.
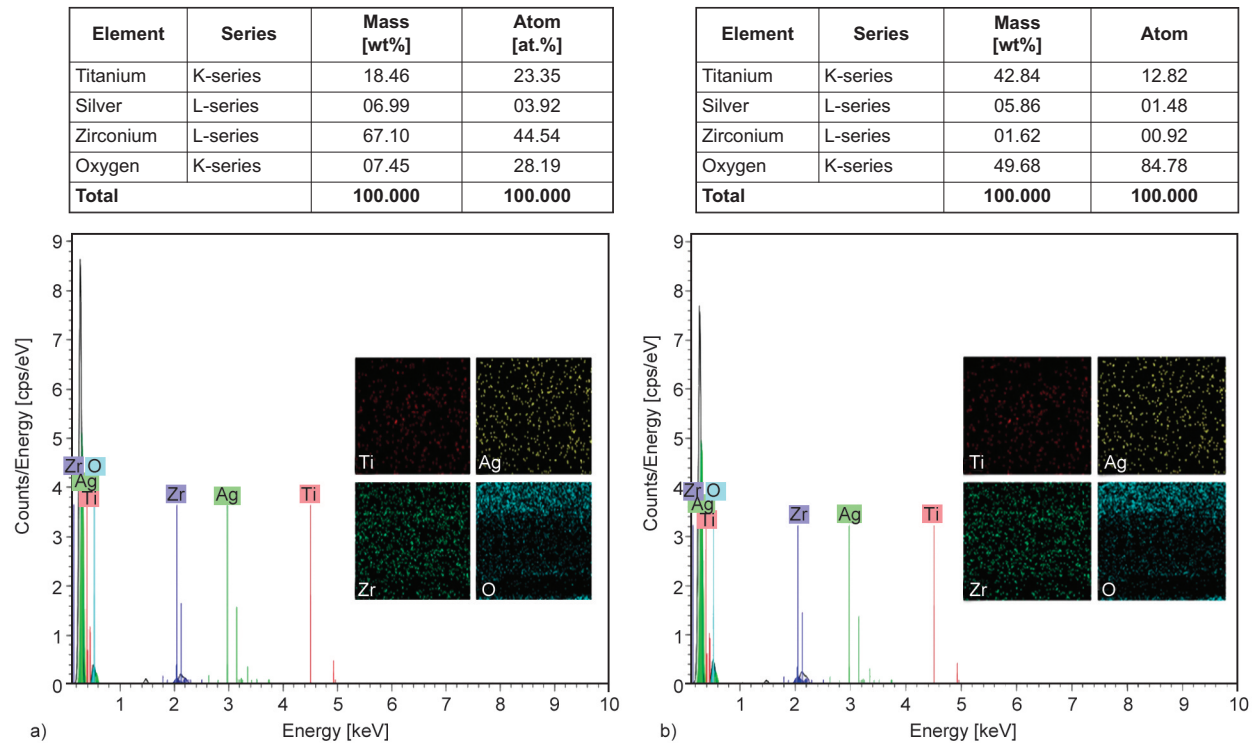
The EDS was used to identify the surface element composition (Figure 8). Before the SEM-EDS image, an Au atom was sputtered onto the substrate. Figure 8 shows the energy-dispersive spectra of the A3ZT particles on the fiber and the sharp peaks of Ag, Zr, and Ti confirming the compositional structure of A3ZT on the fiber. Ag, Zr, and Ti atoms were clearly located on the fiber surface. Ti (red), Ag (yellow), and Zr (green) were distributed on the surface (Figure 8 inset). The elemental distribution on the surface had an influence on the antibacterial activity of the fiber and exhibited significant photocatalytic activity.

3.2.2. The thermal properties

The DSC results for the composite materials confirmed the composition of the sample, including the bicomponent fiber, by comparing the melting temperature with the relative results of the neat PP polymer. The addition of AZT powder to the PP polymer matrices affected the melting temperature (T_m), melting enthalpy (ΔH_m), and crystallization behavior (X_c), which were observed by DSC. The thermal profile used to study. The results data are summarized in Table 2 and Figure 9.

Figure 9a (exotherm) comparison of the PP blend without and with the addition of 1 and 2 wt% of A3ZT powder. T_m of neat PP and T_{mc} of PP1 and PP2 composite fiber were changed with the addition of A3ZT powder based on the values shown in Table 2. T_{mc} of PP1 and PP2 did not significantly change with A3ZT loading. ΔH_m and the degree of crystallinity increased with the addition of A3ZT powder and reached a maximum of 94.93 J/g and 45.86%, respectively. The crystallization temperature of PP is clearly evident in Figure 9b (endotherm) and Table 2. This suggests that the degree of PP crystallinity increased with increasing A3ZT during the extrusion process. As a result, the presence of TiO_2

Element	Series	Mass [wt%]	Atom [at.%]
Titanium	K-series	18.46	23.35
Silver	L-series	06.99	03.92
Zirconium	L-series	67.10	44.54
Oxygen	K-series	07.45	28.19
Total		100.000	100.000

| Element	Series	Mass [wt%]	Atom
Titanium	K-series	42.84	12.82
Silver	L-series	05.86	01.48
Zirconium	L-series	01.62	00.92
Oxygen	K-series	49.68	84.78
Total		100.000	100.000

Figure 8. EDX spectra of the S/C bicomponent fibers, a) PP1/50:50, and b) PP2/50:50.

in PP resulted in an increase in the degree of crystallinity. The crystalline regions contribute to improved mechanical properties, such as tenacity and elongation [35]; however, it is important to note that the specific effect of TiO_2 on crystallinity can depend on various factors, such as the concentration of A3ZT, processing conditions, and compatibility between A3ZT and neat PP.

Bi-componence fiber prepared with and without AZ3T, there were two peaks for all the bicomponent fibers. The first peak, which had a lower temperature, is T_m of PP virgin (core site), whereas the higher peak

represents T_{mc} of the PP/AZT composite (sheath site). The results indicate that the sheath-core ratio affected the melting point. It was altered slightly to a higher degree when the sheath was changed compared with the PP virgin. Furthermore, the X_c was calculated, and the results showed that the X_c of bicomponence fiber was affected by the A3ZT powder in the sheath. With an increased sheath ratio, X_c was reduced when the sheath increased, which affected the mechanical properties of the fiber. Recent studies [26, 36] examining the effect of TiO_2 on thermal properties revealed that TiO_2 significantly affected the
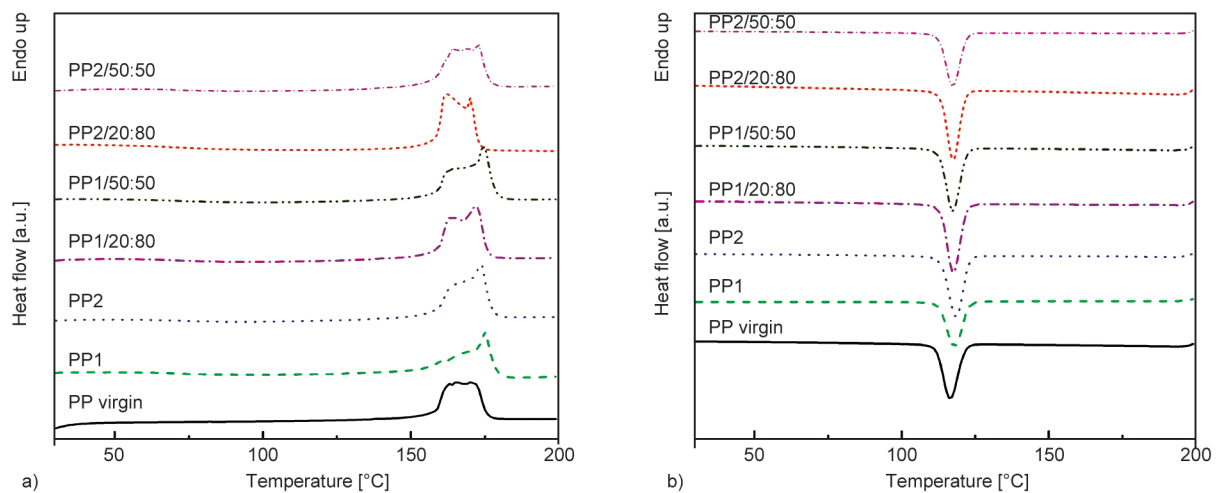
Figure 9. DSC heating (a) and cooling (b) curves.

degree of crystallinity of PP, because TiO_2 is readily dispersed between molecular chains, which damages and prevents the formation of a regular molecular chain structure of PP. Thus, the addition of AZT particles during composite fiber formation results in an effect on the thermal properties. However, the degree of crystallinity can be influenced by various factors, including processing conditions, cooling rates, and the presence of nucleating agents or additives. In addition, the compatibility between the sheath and core components can affect the formation of crystalline regions and the resulting degree of crystallinity.

3.2.3. Mechanical properties

The tenacity and elongation of fibers are shown in Table 2. The tenacity of the PP virgin and PP/A3ZT composite fibers were compared. The tenacity was increased by the addition of A3ZT powder. A3ZT at 2 wt% showed the highest tenacity, indicating good orientation of the PP matrix, whereas at lower concentrations (1 wt% of A3ZT), tenacity was decreased, which suggests that AZT affected the orientation of the PP matrix and the particles indicating reinforcing effect. This corresponded to the degree of X_c, in which X_c of PP2 exhibited the highest degree of crystallinity at 45.86% and tenacity at 3.21±0.41 cN/dtex compared with PP1 having 43.39% crystallinity and 2.59±0.48 cN/dtex tenacity and PP with 42.28% crystallinity and a tenacity of 3.00±0.65 cN/dtex which were lower. On the other hand, elongation of the PP/AZT composite fiber descended in order: PP virgin > PP2 > PP1. The tenacity and elongation properties are dependent upon the degree of PP crystallization. Recent studied [37, 38] indicated that TiO_2 particles can act as nucleating agents, providing sites for the initiation of crystallization and potentially enhance the rate and extent of crystallization. The pres-

ence of nucleating agents can promote the formation of crystalline regions and increase the overall degree of crystallization. However, the impact of TiO_2 as a nucleating agent on the degree of crystallization depends on various factors, including the concentration of TiO_2, processing conditions, and the compatibility between TiO_2 and PP.

For the bicomponent fiber, the tenacity was slightly decreased with increased sheath thickness at a 20 to 50 mass ratio; however, the tenacity of the bicomponent fibers was significantly affected by changes in the C/S ratio. The percentage of crystallinity corresponds to the relative amount of fiber tenacity. PP2/20:80 showed the highest tenacity at 3.11±0.51 cN/dtex, whereas PP1/20:80, PP2/50:50, and PP1/50:50 were lower (Table 2). The elongation at the break of neat PP and bicomponent fiber was reduced by varying the S/C ratio. Compared with neat PP, the bicomponent fiber was at a 20 and 50 ratio in the sheath at 1 and 2 wt%. The elongation at the break of the bicomponent fibers with a PP2:20/80 was the highest; however, using the same AZT content, the elongation at the break decreased as sheath thickness increased. In particular, elongation at the break of a 50/50 (large sheath) bicomponent fiber was lower compared with that of a 20/80 (thin sheath) bicomponent fiber. This may be attributed to the degree of PP crystallization in the sheath, or it could be attributed to the non-uniform distribution of AZT as sheath thickness increased. Here, the results indicated that the elongation properties were increased concomitantly as the degree of crystallization increased (Table 2). With respect to the impact of the sheath and core ratio, the sheath component represented 20% of the AZT composite of the total bicomponent and the core represented 80% of the neat PP. The mechanical properties of the bicomponent

Table 2. Melting temperature, crystallization temperature, melting enthalpy, crystallinity and mechanical properties of PP virgin, PP/AZT composite, and the bicomponent fiber.

Samples name	T_m* [°C]	T_{mc}** [°C]	T_c [°C]	ΔH_m [J/g]	X_c [%]	Tenacity [cN/dtex]	Elongation at break [%]
Virgin PP	165.6	–	116.0	87.51	42.28	3.00±0.65	271.37±23.99
PP1	–	174.9	118.0	69.82	43.39	2.59±0.48	226.06±24.89
PP2	–	173.4	118.5	94.93	45.86	3.21±0.41	265.83±30.27
PP1/20:80	164.9	172.3	117.6	102.10	49.32	3.06±0.32	251.56±26.41
PP1/50:50	163.9	174.4	117.3	96.38	46.56	2.81±0.23	238.53±31.35
PP2/20:80	163.5	170.2	117.5	96.95	46.84	3.11±0.51	252.23±34.83
PP2/50:50	169.1	172.7	117.3	90.95	43.73	2.87±0.38	250.08±21.07

*T_m is melting point of neat PP and
**T_{mc} is melting point of PP/AZT composite

will be primarily governed by the properties of the core. Therefore, it is not surprising that when the sheath increased, elongation decreased.

3.2.4. Antiviral activity of bicomponent fiber

The antiviral activity of the composite fiber and sheath-core bicomponent fiber against SARS-CoV-2 were examined and the results are shown in Table 3. After 30 min of contact, both fibers exhibited strong antiviral activity against SARS-CoV-2. The antiviral activity of the composite fiber increased as A3ZT levels increased. The antiviral activity of the composite fiber at 1 and 2 wt% was 99.81 and 99.86%, with log reduction values of 2.73 and 2.85, respectively under florescent irradiation. The was higher compared with previous studies [39, 40]. SARS-CoV-2 can survive for 48 h on cloth and other studies revealed that fabric coated with an antiviral agent had antiviral activity of 99.38% resulting in a value of 2.21 on logarithmic scale [7]. Considering the S/C bicomponent fiber with different S/C ratios, efficacy increased with increasing S/C ratio. AZT at 2 wt% in the sheath fiber exhibited higher efficacy compared with 1 wt% AZT in all samples; however, viral efficacy did not change significantly when comparing 1 and 2 wt% AZT composite fibers and 1 and 2 wt% ZA3T sheath-core fibers. As a result, the optimal S/C ratio and AZT particle content of the bicomponent fiber for antiviral activity were 50/50 with 2 wt% A3ZT particles. The antivirus mechanism may be due to the interaction of A3ZT on the surface of the sheath fiber with the viral capsid. This suggests that the sheath-core interaction of the fiber with A3ZT particles strengthens the antiviral activity. Because of the susceptibility of A3ZT particles to SARS-CoV-2, the sheath-core bicomponent fiber may play a role in containing the transmission of SARS-CoV-2, particularly in high-risk locations.

4. Conclusions

In this study, the solvothermal method was used to successfully produce Ag and *co*-doped TiO_2. The existence of Ag and Zr doping improved TiO_2 photocatalytic activity under visible light. The XRD pattern and lattice parameter evaluated the interaction of Zr in the TiO_2 lattice. On the other hand, Ag species could be incorporated on the TiO_2 lattice surface in the form of Ag^0 and Ag_2O. The major roles of Zr and Ag on the photocatalytic activities of TiO_2 were different. The Zr doping has a significant influence on trapping and retarded electron-hole pair recombination. Ag-doping has an incredibly significant effect on the narrowing band gap energy of TiO_2, which enhances the light absorption ability toward a visible light region. The *co*-doped photocatalyst of Zr 5% mole and Ag 3% mole (A3ZT) demonstrated synergistic effects, with the highest methylene blue photocatalyst degradation efficiency of up to 93.51% within 8 h under fluorescence light. This could be since AZT showed improved photocatalytic reactivity with synergistic effects by reducing the band gap and inhibiting electron-hole pair recombination. The A3ZT photocatalyst powder was used to prepare bicomponent fiber using the PP matrix. The PP composite TiO_2 *co*-doped with Ag and Zr (A3ZT) was used to produce sheath-core bicomponent fibers with antiviral activity using a double-extrusion, melt-spinning fiber system. The structure of the bicomponent fiber consisted of a PP/AZT composite sheath and a virgin PP core. We generated bicomponent fiber by varying the AZT particle content in the sheath between 1 and 2 wt%, with a sheath-core ratio between 20/80 and 50/50 (w/w). The results indicated that the AZT particles and S/C ratio affected the tensile elongation and thermal properties of PP. The bicomponent fiber killed SARS-CoV-2 in human isolates. An S/C ratio of

Table 3. The antiviral activities of PP/AZT composite fiber and sheath-core bicomponent fibers against SARS-CoV-2.

Sample	15 min		30 min	
	log(reduction)	Efficacy [%]	log(reduction)	Efficacy [%]
PP (100) control	0.900	87.41	1.020	90.45
PP1/20:80	2.610	99.75	2.610	99.75
PP2/50:50	2.610	99.75	2.640	99.77
PP1	2.685	99.79	2.730	99.81
PP2/20:80	2.610	99.75	2.700	99.80
PP2/50:50	2.670	99.79	2.790	99.84
PP2	2.820	99.85	2.850	99.86

50:50 bicomponent fiber with 2 wt% AZT in the sheath was the most effective at killing the virus, resulting in 99.86% eradication within 30 min of contact. This indicates that the bicomponent fiber composite with AZT particles can be used to make antiviral products, such as air filters, gloves, and masks, to stop the spread of coronavirus.

Acknowledgements

References

[1] Kumar A., Singh R., Kaur J., Pandey S., Sharma V., Thakur L., Sati S., Mani S., Asthana S., Sharma T. K., Chaudhuri S., Bhattacharyya S., Kumar N.: Wuhan to world: The COVID-19 pandemic. Frontiers in Cellular and Infection Microbiology, **11**, 596201 (2021).
https://doi.org/10.3389/fcimb.2021.596201

[2] Jayaweera M., Perera H., Gunawardana B., Manatunge J.: Transmission of COVID-19 virus by droplets and aerosols: A critical review on the unresolved dichotomy. Environmental Research, **188**, 109819 (2020).
https://doi.org/10.1016/j.envres.2020.109819

[3] Chakraborty I., Maity P.: COVID-19 outbreak: Migration, effects on society, global environment and prevention. Science of the Total Environment, **728**, 138882 (2020).
https://doi.org/10.1016/j.scitotenv.2020.138882

[4] Alimohamadi Y., Sepandi M., Taghdir M., Hosamirudsari H.: Determine the most common clinical symptoms in COVID-19 patients: A systematic review and meta-analysis. Journal of Preventive Medicine Hygiene, **61**, E304–E312 (2020).
https://doi.org/10.15167/2421-4248/jpmh2020.61.3.1530

[5] Fu J., Liu T., Touhid S. S. B., Fu F., Liu X.: Functional textile materials for blocking COVID-19 transmission. ACS Nano, **17**, 1739–1763 (2023).
https://doi.org/10.1021/acsnano.2c08894

[6] Jung S., Yang J-Y., Byeon E-Y., Kim D-G., Lee D-G., Ryoo S., Lee S., Shin C-W., Jang H. W., Kim H. J., Lee S.: Copper-coated polypropylene filter face mask with SARS-CoV-2 antiviral ability. Polymers, **13**, 1367 (2021).
https://doi.org/10.3390/polym13091367

[7] Weber S. S., Bulliard X., Bonfante R., Xiang Y., Biselli S., Steiner S., Constant S., Pugin R., Laurent A., Majeed S., Lebrun S., Palmieri M., Hogg A., Kuczaj A., Peitsch M. C., Hoeng J., Stan A.: *In vitro* testing of salt coating of fabrics as a potential antiviral agent in reusable face masks. Scientific Reports, **12**, 17041 (2022).
https://doi.org/10.1038/s41598-022-21442-7

[8] Abazari M., Badeleh S. M., Khaleghi F., Saeedi M., Haghi F.: Fabrication of silver nanoparticles-deposited fabrics as a potential candidate for the development of reusable facemasks and evaluation of their performance. Scientific Reports, **13**, 1593 (2023).
https://doi.org/10.1038/s41598-023-28858-9

[9] Qiu Q., Yang C., Wang Y., Alexander C. A., Yi G., Zhang Y., Qin X., Yang Y. Y.: Silane-functionalized polyionenes-coated cotton fabrics with potent antimicrobial and antiviral activities. Biomaterials, **284**, 121470 (2022).
https://doi.org/10.1016/j.biomaterials.2022.121470

[10] Zhang Y., Fan W., Sun Y., Chen W., Zhang Y.: Application of antiviral materials in textiles: A review. Nanotechnology Reviews, **10**, 1092–1115 (2021).
https://doi.org/10.1515/ntrev-2021-0072

[11] Vijayan P. P., Chithra P. G., Abraham P., George J. S., Maria H. J., Sreedevi T., Thomas S.: Nanocoatings: Universal antiviral surface solution against COVID-19. Progress in Organic Coatings, **163**, 106670 (2022).
https://doi.org/10.1016/j.porgcoat.2021.106670

[12] Prakash J., Cho J., Mishra Y. K.: Photocatalytic TiO$_2$ nanomaterials as potential antimicrobial and antiviral agents: Scope against blocking the SARS-CoV-2 spread. Micro and Nano Engineering, **14**, 100100 (2022).
https://doi.org/10.1016/j.mne.2021.100100

[13] Pivsa-Art S., Sunyikhan K., Pivsa-Art W.: Bicomponent multifilament yarns of recycled poly(ethylene terephthalate) and nano-titanium dioxide for antibacterial carpet. Journal of Industrial Textiles, **51**, 1034S–1047S (2021).
https://doi.org/10.1177/15280837211011774

[14] Dhabarde N., Khaiboullina S., Uppal T., Adhikari K., Verma S. C., Subramanian V. R.: Inactivation of SARS-CoV-2 and other human coronaviruses aided by photocatalytic one-dimensional titania nanotube films as a self-disinfecting surface. ACS Applied Material Interfaces, **14**, 50463–50474 (2022).
https://doi.org/10.1021/acsami.2c03226

[15] Jaggessar A., Velic A., Yarlagadda P. K., Spann K.: TiO$_2$ nanostructures that reduce the infectivity of human respiratory viruses including SARS-CoV-2. ACS Biomaterials Science and Engineering, **8**, 2954–2959 (2022).
https://doi.org/10.1021/acsbiomaterials.2c00326

[16] Wu S., Ishisone K., Sheng Y., Manuputty M. Y., Kraft M., Xu R.: TiO$_2$ with controllable oxygen vacancies for efficient isopropanol degradation: Photoactivity and reaction mechanism. Catalysis Science and Technology, **11**, 4060–4071 (2021).
https://doi.org/10.1039/d1cy00417d

[17] Binas V., Venieri D., Kotzias D., Kiriakidis G.: Modified TiO$_2$ based photocatalysts for improved air and health quality. Journal of Materiomics, **3**, 3–16 (2017).
https://doi.org/10.1016/j.jmat.2016.11.002

[18] Aqeel M., Ikram M., Imran M., Ul-Hamid A., Qumar U., Shahbaz A., Ikram M., Saeed A.: TiO$_2$ *co*-doped with Zr and Ag shows highly efficient visible light photocatalytic behavior suitable for treatment of polluted water. RSC Advances, **10**, 42235–42248 (2020).
https://doi.org/10.1039/D0RA08718A

[19] Zhang D., Hu H., Wei J-A., Xu X., Chen L., Wu X., Yu Q., Zhang B-X., Wang L.: Zr-doped TiO$_2$ ceramic nanofibrous membranes for enhancing photocatalytic organic pollutants degradation and antibacterial activity. Colloids and Surfaces A: Physicochemical and Engineering Aspects, **665**, 131231 (2023).
https://doi.org/10.1016/j.colsurfa.2023.131231

[20] Wardhana A. C., Yasuhara S., Yu M-W., Yamaguchi A., Nagao T., Ishii S., Miyauchi M.: Direct imaging of visible-light-induced one-step charge separation at the chromium(III) oxide–strontium titanate interface. Journal of Materials Chemistry A, **10**, 752–761 (2022).
https://doi.org/10.1039/D1TA08950A

[21] Obaiah G. O., Kemparajegowda, Gireesha J., Mylarappa M.: Comparative study of TiO$_2$ and palladium doped TiO$_2$ nano catalysts for water purification under solar and ultraviolet irradiation. Chemistry of Inorganic Materials, **1**, 100002 (2023).
https://doi.org/10.1016/j.cinorg.2023.100002

[22] Guo Z., Jing G., Tolba S. A., Yuan C-S., Li Y-H., Zhang X., Huang Z., Zhao H., Wu X., Shen H., Xia W.: Design and construction of an O-Au-O coordination environment in Au single atom-doped Ti^{4+} defected TiO$_2$ for an enhanced oxidative ability of lattice oxygen for Hg$_0$ oxidation. Chemical Engineering Journal, **451**, 138895 (2023).
https://doi.org/10.1016/j.cej.2022.138895

[23] Sukhadeve G. K., Bandewar H., Janbandhu S. Y., Jayaramaiah J. R., Gedam R. S.: Photocatalytic hydrogen production, dye degradation, and antimicrobial activity by Ag-Fe *co*-doped TiO$_2$ nanoparticles. Journal of Molecular Liquids, **369**, 120948 (2023).
https://doi.org/10.1016/j.molliq.2022.120948

[24] Sanitnon P., Chiarakorn S., Chawengkijwanich C., Chuangchote S., Pongprayoon T.: Synergistic effects of zirconium and silver *co*-dopants in TiO$_2$ nanoparticles for photocatalytic degradation of an organic dye and antibacterial activity. Journal of the Australian Ceramic Society, **56**, 579–590 (2020).
https://doi.org/10.1007/s41779-019-00368-w

[25] Standard I.: Textiles - Determination of antiviral activity of textile products, ISO 18184:2019(e). (2019).

[26] Bendaoued A., Messaoud M., Harzallah O., Bistac S., Salhi R.: Nano-TiO$_2$ effect on thermal, rheological and structural properties of thermoplastic polypropylene nanocomposites. Journal of Materials Research and Technology, **17**, 2313–2325 (2022).
https://doi.org/10.1016/j.jmrt.2022.01.114

[27] Li W., Liang R., Hu A., Huang Z., Zhou Y. N.: Generation of oxygen vacancies in visible light activated one-dimensional iodine TiO$_2$ photocatalysts. RSC Advances, **4**, 36959–36966 (2014).
https://doi.org/10.1039/C4RA04768K

[28] Tian H., Zhang Z-Y., Liu C-Y.: Construction of needle-like crystalline ago ordered structures from Ag nanoparticles and their properties. New Journal of Chemistry, **42**, 5376–5381 (2018).
https://doi.org/10.1039/C7NJ05007K

[29] Gonell F., Portehault D., Julián-López B., Vallé K., Sanchez C., Corma A.: One step microwave-assisted synthesis of nanocrystalline WO$_X$–ZrO$_2$ acid catalysts. Catalysis Science and Technology, **6**, 8257–8267 (2016).
https://doi.org/10.1039/C6CY01082B

[30] Guan S-H., Li Y-F., Liu Z-P.: Structural origin for the enhanced photocatalysis of Zr–Ti oxide composites from machine learning. The Journal of Physical Chemistry C, **127**, 22537–22547 (2023).
https://doi.org/10.1021/acs.jpcc.3c04177

[31] Sirivallop A., Areerob T., Chiarakorn S.: Enhanced visible light photocatalytic activity of N and Ag doped and *co*-doped TiO$_2$ synthesized by using an *in-situ* solvothermal method for gas phase ammonia removal. Catalysts, **10**, 251 (2020).
https://doi.org/10.3390/catal10020251

[32] Dey D., Halder N., Misra K. P., Chattopadhyay S., Jain S. K., Bera P., Kumar N., Mukhopadhyay A. K.: Systematic study on the effect of Ag doping in shaping the magnetic properties of sol-gel derived TiO$_2$ nanoparticles. Ceramics International, **46**, 27832-27848 (2020).
https://doi.org/10.1016/j.ceramint.2020.07.282

[33] Puspitarum D. L., Istiqomah N. I., Larasati D. A., Kusumaatmaja A., Aliah H., Suharyadi E.: Photocatalytic mechanism and properties of recyclable hybrid magnetic/semiconductor nanocomposites synthesized *via* green route for organic dye degradation. Results in Materials, **19**, 100439 (2023).
https://doi.org/10.1016/j.rinma.2023.100439

[34] Pavel M., Anastasescu C., State R-N., Vasile A., Papa F., Balint I.: Photocatalytic degradation of organic and inorganic pollutants to harmless end products: Assessment of practical application potential for water and air cleaning. Catalysts, **13**, 380 (2023).
https://doi.org/10.3390/catal13020380

[35] Roiron C., Lainé E., Grandidier J-C., Garois N., Vix-Guterl C.: A review of the mechanical and physical properties of polyethylene fibers. Textiles, **1**, 86–151 (2021).
https://doi.org/10.3390/textiles1010006

[36] Awang M., Wan Mohd W. R., Sarifuddin N.: Study the effects of an addition of titanium dioxide (TiO$_2$) on the mechanical and thermal properties of polypropylene-rice husk green composites. Materials Research Express, **6**, 075311 (2019).
https://doi.org/10.1088/2053-1591/ab1173

[37] Triamnak N., Suttiruengwong S., Vittayakorn N., Girdthep S., Khankrua R.: The properties investigations of PLA/TiO$_2$ and PLA/doped-TiO$_2$ composites films. Polymer-Plastics Technology and Materials, **62**, 1576–1586 (2023).
https://doi.org/10.1080/25740881.2023.2222818

[38] Prakash M., Ghosh A. K.: Rheology-cell structure correlation for foam processing of polypropylene-titanium dioxide and polypropylene-graphene nanocomposites. Polymer Engineering and Science, **63**, 4174–4185 (2023).
https://doi.org/10.1002/pen.26516

[39] Riddell S., Goldie S., Hill A., Eagles D., Drew T. W.: The effect of temperature on persistence of SARS-CoV-2 on common surfaces. Virology Journal, **17**, 145 (2020).
https://doi.org/10.1186/s12985-020-01418-7

[40] SadrHaghighi A., Sarvari R., Fakhri E., Poortahmasebi V., Sedighnia N., Torabi M., Mohammadzadeh M., Azhiri A. H., Eskandarinezhad M., Moharamzadeh K., Keyhanvar P.: Copper-nanoparticle-coated melt-blown facemask filter with antibacterial and SARS-CoV-2 antiviral ability. ACS Applied Nano Materials, **6**, 12849–12861 (2023).
https://doi.org/10.1021/acsanm.3c01471